Volume 1 | Number 1 | Jan 2013 | Pages 1–100

Nanoscale

www.rsc.org/nanoscale

ROYAL SOCIETY OF CHEMISTRY

ROYAL SOCIETY OF CHEMISTRY

www.rsc.org/nanoscale

Nanoscale

ARTICLE

Hydrogen sorption properties of Pd-Co nanoalloys embedded into mesoporous carbons

Claudia Zlotea[a], Camelia Matei Ghimbeu[b], Yassine Oumellal[a], Jean-Claude Crivello[a], Cathie Vix-Guterl[b] and Michel Latroche[a]

$Pd_{90}Co_{10}$ and $Pd_{75}Co_{25}$ nanoalloys embedded into mesoporous carbon hosts have been prepared by two synthetic methods: direct and indirect. The average nanoparticles size can be tuned by both the temperature during thermal treatment and the chemical composition: the higher treatment temperature and richer Pd composition, the larger nanoparticles size. Twofold size- and composition-dependence of the hydrogen sorption properties at room temperature are evidenced. The Co substitution in Pd nanoalloys increases the equilibrium pressure at room temperature relative to nanosized Pd. The hydrogen sorption capacity decreases by Co substitution in Pd, as also demonstrated by SQS+DFT calculations.

Introduction

Among noble metals, Pd is the only element that absorbs hydrogen at ambient temperature and pressure forming an interstitial metallic hydride $PdH_{0.67}$. For this reason, bulk Pd is the most studied element for hydrogen storage and is one of the best understood metal-hydrogen system.[1] As Pd is a rather expensive element, binary Pd alloys have been extensively studied to develop more economically feasible storage materials.[2–7] The aim was to improve both the hydrogen storage capacity and the thermodynamics. For example, an increase of the equilibrium plateau pressure together with a decrease of the capacity with increasing Co concentration are reported in bulk Pd-Co *fcc* substitutional alloys (maximum Co solubility of 15 at%).[2,4,6] This behaviour was explained in terms of lattice volume change by Co substitution. The plateau pressures of "contracted" Pd-based alloys (whose units cells are smaller than that of pure Pd) are higher than that of Pd-H.[4] Moreover, an almost linear dependence of the thermodynamic parameters of the Pd-Co binary alloys was proposed in the literature as function of lattice parameters.[5] However, only steric effect cannot entirely account for this behaviour, electronic features of alloys might also play an important role in the thermodynamics. A simplistic model based on the rigid band model of the electronic structure was proposed earlier for the Pd-H system.[7] This electronic description is based on the filling of unoccupied *d* states of Pd with electrons supplied by dissolved hydrogen atoms. However, the link between the electronic structure of Pd-based alloys and their hydrogen

storage capabilities is less straightforward.[8]

Due to the recent development of nanotechnology, downscaling of the active material particle dimensions to nanometre range has become a promising approach to tailor hydrogen storage properties of materials.[9] Consequently, Pd has become the model material to study the nanosizing effect on metal-hydrogen interaction.[10–14] At nanoscale, metal particles need to be stabilized against coalescence by confinement into either porous scaffolds or surfactants. The use of porous scaffolds is most widespread due to available pores with tailored dimensions that serve as both nanoreactors for confining the synthetic reaction of nanoparticles and nanomoulds for the synthesized species. Hence, along with nanosizing, nanoconfinement effects on hydrogen sorption properties of nanoparticles have been also reported.[15,16]

The most obvious nanosize/nanoconfinement effect for Pd is observed in the pressure-composition-isotherms (PCI).[17,18] The hydrogen solubility in the solid solution (α phase) increases by decreasing the size while the hydrogen solubility in the hydride phase (β phase) decreases with decreasing the size. Accordingly, the miscibility gap (two-phase region) narrows by decreasing the particle size.[17,19] These results have been confirmed by *in situ* XRD on Pd nanoparticles with different average sizes.[11,14,15]

In this context, Pd-based nanoalloys provide excellent systems to explore combined effect of alloying and nanosizing/nanoconfinement on the properties of materials for solid-state hydrogen storage. To our knowledge, one previous paper has reported hydrogen sorption properties of a Pd-Ni nanoalloy embedded into a carbon host[20], whereas supported Pd-Co nanoalloys have been only studied for their catalytic properties in different chemical reactions.[21–23]

The purpose of this work is to determine the hydrogen sorption properties of different Pd-Co nanoalloys embedded

[a] *Institut de Chimie et des Matériaux Paris-Est, CNRS UMR 7182, UPEC, 2-8 rue Henri Dunant, 94320 Thiais, France*
[b] *Institut de Science des Matériaux de Mulhouse, CNRS UMR 7361, UHA, 15 rue Jean Starcky, 68057 Mulhouse, France*

into mesoporous carbon supports. From the synthetic point of view, the preparation of alloy nanoparticles directly into the pores of a scaffold remains a paramount challenge. We have synthesized $Pd_{90}Co_{10}$ and $Pd_{75}Co_{25}$ nanoalloys with different average sizes using two different methods: indirect and direct. The first method was used to prepare nanoalloys embedded into carbon scaffolds by a lengthy multiple steps route, whereas the latter one was employed to rapidly synthesize both nanoalloys and carbon host in a single step. Twofold composition and size effects are highlighted on the fundamental and hydrogen sorption properties. These properties are compared to the bulk alloys counterparts to enlighten the modifications introduced by nanosizing and/or nanoconfinement. Discussion is supported by combined approach based on the Special Quasi-random Structure (SQS) method and the Density Functional Theory (DFT) calculations to understand the electronic band structure of bulk *fcc* Pd-Co solid solutions.

Experimental and calculation details

Synthesis of carbons and composite materials

The composite materials have been synthesized following two routes: the direct method at high temperature (600 °C) and the indirect one at two different temperatures (300 and 500 °C). Two Pd-Co compositions were selected: $Pd_{90}Co_{10}$ and $Pd_{75}Co_{25}$. Thus, a total of six composites were prepared and further named $Pd_{100-x}Co_x@C\text{-}T$, where x is the Co composition (10 or 25 at%) and T is the treatment temperature during synthesis.

The direct method is based on a soft-template approach, which relies on the evaporation induced self-assembly (EISA) of an ethanolic solution containing carbon precursors (phloroglucinol/glyoxal), a soft-template (Pluronic 127) and metallic salts.[24] Briefly, the phloroglucinol and Pluronic 127 were dissolved in ethanol under stirring followed by addition of glyoxal, $Co(NO_3)_2\cdot6H_2O$ and $PdCl_2$ priory dissolved in concentrated HCl (37 vol%), respectively. The as-obtained solution was placed in petri dishes for evaporation, followed by thermopolymerization (80°C, 12h) and thermal treatment at 600°C under argon. The thermal treatment allows the decomposition of the template with the formation of porosity, the carbonization of precursors and the decomposition of the metallic salts with the *in situ* formation of metal nanoalloys in the carbon matrix. No hydrogen reducing agent is required since the carbon is playing the role of reducing agent.

The indirect method is a three step procedure: first, the carbon hosts were prepared by soft template route followed by impregnation with an aqueous solution of a mixture of metal precursors and subsequently reduced under Ar/H_2 flow. For the preparation of carbon hosts with 3.5 and 7.0 nm average pore sizes the same carbon precursors (phloroglucinol/glyoxal) and soft-template (Pluronic) were used and dissolved in a mixture ethanol/HCl. The obtained solution was casted in two different ways. To obtain the carbon with large pores (7.0 nm) the solution was left aging for

3 days until a phase separation (polymer rich/ethanol) took place.[25] To prepare the 3.5 nm pore size carbon, the same solution was disposed in petri dishes and evaporated.[26] Both resulting polymers were cured at 80 °C and thermally treated at 900 °C in Ar.

The as prepared carbon hosts were impregnated with aqueous solution of mixed $Co(NO_3)_2$ and H_2PdCl_4 metal precursors at room temperature. The dried mixture was subsequently reduced under Ar/H_2 flow (0.5 mL/min) at 300 and 500 °C for 3 hours. To ensure an appropriate confinement of particles within the porous host, the carbons with 3.5 and 7.0 nm pore sizes were chosen for the preparation of the composites at 300 and 500 °C, respectively.

Characterizations

Chemical, structural, microstructural and textural properties

The chemical compositions of the composites have been determined by inductively coupled plasma optical emission spectrometry (ICP-OES) and the results are listed in Table 1.

The structural properties of pristine carbons and composites have been determined by X-ray powder diffraction (XRD) using a D8 advanced Bruker diffractometer (Cu K_α radiation, Bragg-Brentano geometry). To characterize the crystallographic changes induced by hydrogen absorption, *in situ* XRD measurements were performed by stepwise increase of hydrogen pressures at ambient temperature. The samples were initially evacuated under primary vacuum and hydrogen pressure was incremented up to 0.1 MPa. The XRD patterns have been analyzed using the TOPAS software (Bruker AXS Topas 4.2) to determine the lattice parameters and the crystallite sizes of the Pd-Co nanoparticles (if applicable).

The microstructural observations were performed by Transmission Electron Microscopy (TEM) with a 200 kV FEG TEM (FEI Tecnai F20 equipped with a Gatan energy Imaging Filter, resolution 0.24 nm). The Pd-Co nanoparticles size distribution and average size have been determined by statistical analyses of several TEM images.

The textural properties of the composites have been determined by nitrogen adsorption isotherms at liquid nitrogen temperature (-196 °C) using an Autosorb IQ Quantachrome instrument and an Micromeritics ASAP 2020 set-up. Prior to measurements, the samples have been degassed under vacuum at 200 °C for 12 h. The specific surface area was obtained by the Brunauer-Emmett-Teller (BET) method within the 0.05-0.25 relative pressure range and the total porous volume was calculated at a relative pressure P/P_0 = 0.95. The textural properties of the pristine carbons and the six composites are given per gram of total mass (Table 1).

Hydrogen sorption properties

Hydrogen sorption properties were determined by measuring the Pressure-Composition-Isotherm (PCI) curves at 20 °C up to 0.1 MPa hydrogen pressure using an automated volumetric device (Autosorb IQ Quantachrome). Prior to any sorption measurement, the samples were pre-treated under hydrogen atmosphere at 20 °C to reduce oxides at the surface of nanoparticles and subsequently degassed at 120 °C to remove water molecules formed during oxide reduction.[27] The PCI

Sample	Carbon / Composite pore size (nm)	Synthetic method and T (°C)	Metal composition ICP-OES (wt%)	Pd/Co stoichiometry ICP-OES (at%)	S_{BET} (m^2/g)	V_t (cm^3/g)	Average size of crystallites / particles (nm)	
							XRD	TEM
Carbon 3.5	3.5	Soft template 600	-	-	781	0.67	-	-
Carbon 7.0	7.0	Soft template 600	-	-	726	0.82	-	-
$Pd_{90}Co_{10}$@C-300	3.5	Indirect 300	8.8	89.2/10.8	747	0.63	-	2.4
$Pd_{75}Co_{25}$@C-300	3.5	Indirect 300	8.3	74.5/25.5	702	0.57	-	2.1
$Pd_{90}Co_{10}$@C-500	7.0	Indirect 500	9.5	89.2/10.8	710	0.82	6.2	6.4
$Pd_{75}Co_{25}$@C-500	7.0	Indirect 500	9.5	75.5/24.5	719	0.85	6.0	5.3
$Pd_{90}Co_{10}$@C-600	3.5	Direct 600	4	-	817	0.54	17	23
$Pd_{75}Co_{25}$@C-600	3.5	Direct 600	4	75.7/24.3	848	0.60	10	12.5

Table 1. Synthetic details, chemical, textural and microstructural properties of Pd-Co composites and pristine carbons.

curves were measured twice (*i.e.* two full adsorption-desorption cycles) with a good measurement repeatability.

Theoretical calculations by SQS/DFT

The binary Pd-Co *fcc* solid solution has been treated by the SQS method[28]: a random-like distribution of Co and Pd atoms into the bulk *fcc* lattice is considered at a given composition and with a finite number of total atoms in a cell. The choice was made by considering a 16-atom cell in SQS structure for 3 compositions (¼, ½, ¾)[29], and infinite dilution ($^1/_{16}$, $^{15}/_{16}$). These structures have been calculated in the frame of the DFT within a pseudo-potential approach using the VASP package.[30,31] The PBE functional has been used with a 400 eV cut-off energy[32] and a high k-mesh density. Preserving the original crystal symmetry, each structure has been fully relaxed, with and without the electronic spin-polarization.
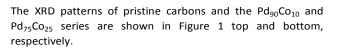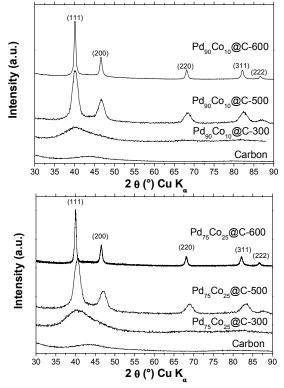
Results

Chemical, textural, structural and microstructural properties

Synthetic details, chemical compositions and textural properties of the six composites and the two pristine carbons are listed in Table 1.

The chemical analysis confirm that the composites contain around 9 and 4 wt.% of metals for samples prepared by indirect and direct method, respectively. The Pd-Co nanoparticles prepared by the indirect method have approximately 90:10 and 75:25 compositions.

Both BET surface area and total porous volume trend to decrease after the formation of nanoparticles by both direct and indirect methods, as already noticed for other similar composites. [18,24,33]

The XRD patterns of pristine carbons and the $Pd_{90}Co_{10}$ and $Pd_{75}Co_{25}$ series are shown in Figure 1 top and bottom, respectively.

Figure 1. XRD patterns of $Pd_{90}Co_{10}$ series (top): $Pd_{90}Co_{10}$@C-300, $Pd_{90}Co_{10}$@C-500, $Pd_{90}Co_{10}$@C-600 and $Pd_{75}Co_{25}$ series (bottom): $Pd_{75}Co_{25}$@C-300, $Pd_{75}Co_{25}$@C-500, $Pd_{75}Co_{25}$@C-600. The Miller indexes of the diffraction peaks from the *fcc* structure are also indicated.
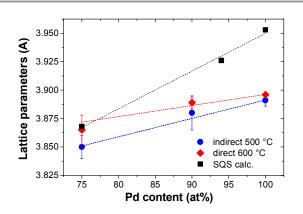
Figure 2. Lattice parameters of the *fcc* Pd-Co nanoalloys prepared at 500 and 600 °C, as determined experimentally (red and blue symbols) and as obtained by SQS calculation (black symbols).

The mesoporous carbons show low degree of graphitization, as suggested by the broad diffraction peaks, irrespective of their pore size dimensions. No diffraction peaks from pure Co could be noticed in the XRD patterns. Both nanoalloys reduced at 300 °C show only a broad diffraction peak around 40 ° corresponding to the overlapping of (111) and (200) peaks of the *fcc* structure. Their lattice parameters could not be determined due to strong overlapping of peaks.

All nanoalloys synthesized at 500 and 600 °C crystallize within a *fcc* structure, characteristic for Pd-Co substitutional alloys.[6] The full width at half maximum (FWHM) of the diffraction peaks becomes narrower with increasing the temperature during thermal treatment, regardless of the Pd-Co composition. This points out larger crystallite sizes with increasing the treatment temperature, as confirmed by structural refinements (Table 1).

The *fcc* lattice parameters of Pd-Co nanoalloys, as obtained

experimentally and calculated by SQS method, are plotted in Figure 2 and compared to those of pure Pd nanoparticles.

A linear decrease of experimental lattice parameters is noticed with increasing the Co content, in good agreement with previously reported bulk and nanosized Pd-Co alloys.[6,22] Similar trend is noticed in the relaxed lattice parameters calculated by SQS calculations, although they are slightly overestimated relative to experimental values. The shrink in lattice parameter is due to smaller Co atomic size relative to Pd. Because the Pd-Co phase diagram is fully miscible (complete *fcc* solid solutions), this results proves that Pd-Co nanoalloys embedded into porous carbons are formed by both indirect route at 500 °C and direct method at 600 °C, irrespective of their composition.

Typical TEM images of the $Pd_{90}Co_{10}$ and $Pd_{75}Co_{25}$ series are shown in Figure 3 top and bottom, respectively. Pd-Co nanoparticles are well distributed within the carbon porous hosts, irrespective of synthetic method and the carbon host. In the case of direct method, nanoalloys are faceted and show different polyhedral shapes.

The average particle sizes, as determined by TEM analysis, are listed in Table 1. A good agreement is observed between the crystallite sizes obtained by XRD refinements (TOPAS refinements) and the average particle sizes determined by TEM for the composites prepared at 500 and 600 °C.

The average sizes of nanoparticles increase with the thermal treatment, as already established in our previous study on pure Pd nanoparticles.[18] Moreover, the average sizes of Pd-Co nanoalloys decrease with increasing the Co content for the same treatment temperature, in good agreement with earlier study on Pd-Co nanoalloys obtained by ultrasonic spray method.[22]

Only from XRD patterns of composites prepared at 300 °C, the confirmation of the formation of Pd-Co nanoalloy is not
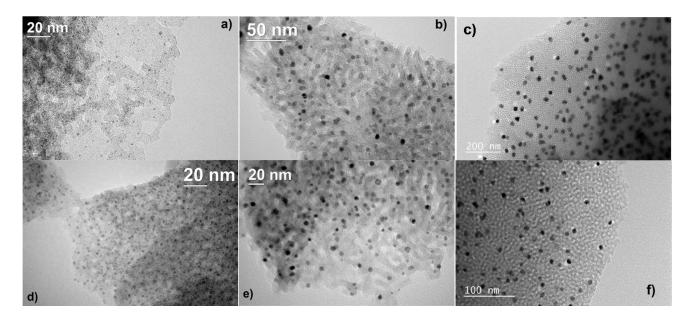

Figure 3. TEM images of $Pd_{90}Co_{10}$@C-300 (a), $Pd_{90}Co_{10}$@C-500 (b), $Pd_{90}Co_{10}$@C-600 (c), $Pd_{75}Co_{25}$@C-300 (d), $Pd_{75}Co_{25}$@C-500 (d) and $Pd_{75}Co_{25}$@C-600 (f).

straightforward. However, from our previous results on pure Pd nanoparticles (also reduced at 300 °C)[11] and the present TEM analysis, the average particle size diminishes with the Co composition: 3.0, 2.4 to 2.1 nm for pure Pd, $Pd_{90}Co_{10}$ and $Pd_{75}Co_{25}$, respectively. This composition-dependence of particle size evidences that Pd-Co nanoalloys are formed even at such low temperature.
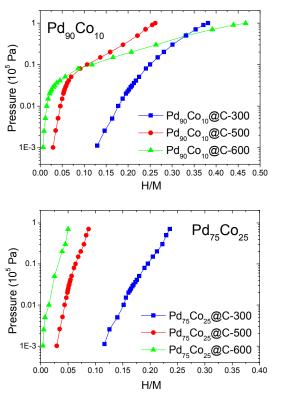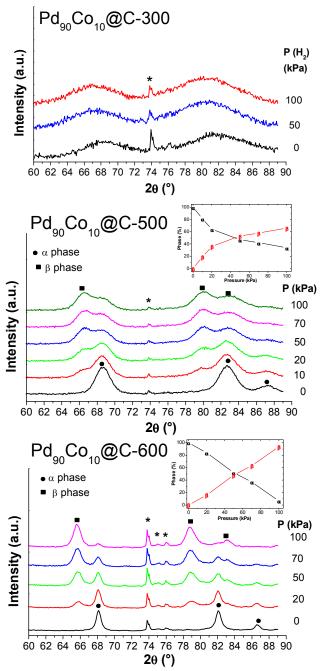

Figure 4. Pressure-Composition-Isotherms at 20 °C for both $Pd_{90}Co_{10}$ (top) and $Pd_{75}Co_{25}$ (bottom) series.

Hydrogen sorption properties

PCI curves of both $Pd_{90}Co_{10}$ and $Pd_{75}Co_{25}$ series are plotted in Figure 4 top and bottom, respectively. As already demonstrated for similar Pd-based composites, the hydrogen sorption at room temperature up to 0.1 MPa H_2 pressure can be entirely attributed to absorption into nanoparticles since the adsorption on the porous carbon supports is negligible.[11,14,27]

The PCI curves for the six composites are completely reversible under the present experimental conditions (not shown). Two samples $Pd_{90}Co_{10}@C-500$ and $Pd_{90}Co_{10}@C-600$ show the presence of sloped plateau with a steeper shape for $Pd_{90}Co_{10}@C-500$. This proves the formation of a hydride phase for both $Pd_{90}Co_{10}$ nanoalloys with average particle sizes of 23 and 6.4 nm. Both plateaus start at around 5 kPa without an apparent end at 0.1 MPa, which indicates that the nanoalloys are not completely hydrogenated at 0.1 MPa. The maximum capacities are 0.26 and 0.46 H/M for $Pd_{90}Co_{10}@C-500$ and $Pd_{90}Co_{10}@C-600$, respectively.

In the case of $Pd_{90}Co_{10}@C-300$, which has the smallest average particles size among the $Pd_{90}Co_{10}$ series, the presence of a plateau pressure is less obvious. The $Pd_{75}Co_{25}$ nanoalloy series form only solid solutions with hydrogen, notwithstanding the average size.

To confirm the PCI results, *in situ* XRD measurements have been performed on both $Pd_{90}Co_{10}$ and $Pd_{75}Co_{25}$ series under similar experimental conditions.

Figure 5. *In situ* XRD during hydrogen absorption of $Pd_{90}Co_{10}@C-300$ (top), $Pd_{90}Co_{10}@C-500$ (middle) and $Pd_{90}Co_{10}@C-600$ (bottom) at 20 °C. The diffraction peak marked with * belongs to the metallic sample holder. For $Pd_{90}Co_{10}@C-500$ (middle) and $Pd_{90}Co_{10}@C-600$ (bottom), the α and β phase evolution versus H2 pressure are also shown (inset).

In situ XRD of $Pd_{90}Co_{10}@C$-300, $Pd_{90}Co_{10}@C$-500 and $Pd_{90}Co_{10}@C$-600 are shown in Figure 5. For $Pd_{90}Co_{10}@C$-500 and $Pd_{90}Co_{10}@C$-600, the α and β phase evolution versus H_2 pressure are also plotted, as determined by TOPAS structural refinements. For the $Pd_{75}Co_{25}$ series, no conclusive results have been obtained by *in situ* XRD (figure not shown).

The $Pd_{90}Co_{10}$ nanoalloy synthesized at 600 °C shows the formation of small extra diffraction peaks at lower 2θ angles already at 20 kPa. These peaks are originating from the β hydride (*fcc* phase) and reinforce with increasing H_2 pressure at the expenses of the α phase. The peaks of the metallic sample holder (marked with *) play the role of an internal standard that do not change with H_2 pressure confirming that the observed peak shift is due to hydrogen absorption into $Pd_{90}Co_{10}$ nanoalloy. This nanoalloy almost completely transforms into the hydride phase (5% of α phase still remaining at 0.1 MPa), as proven by structural refinements (Figure 5). This finding is in agreement with PCI curve showing an incomplete hydride transformation at 0.1 MPa.

The $Pd_{90}Co_{10}$ nanoalloy synthesized at 500 °C has broader diffraction peaks (Figure 5) due to smaller average particle size (6.4 nm), as compared to the same nanoalloy at 600 °C (23 nm). From *in situ* XRD, hydrogen absorption is similar to the previous case: a *fcc* hydride phase is formed already at 10 kPa and the nanoalloy is not completely transformed into the β phase since 34 % of α phase is still present at 0.1 MPa (Figure 5). This is in accord with the sloped plateau pressure and incomplete formation of hydride at 0.1 MPa found in the PCI curve.

For the $Pd_{90}Co_{10}$ nanoalloy synthesized at 300 °C, small displacement of diffraction peaks to lower 2θ angles is observed with increasing H_2 pressure (Figure 5). However, it is impossible to discriminate between the formation of a solid solution or a hydride phase because of broad and strongly overlapping diffraction peaks.

The *in situ* XRD results are in very good agreement with the PCI curves for the $Pd_{90}Co_{10}$ series.

SQS/DFT calculations

As an example, the density of states (DOS) of the bulk $Pd_{75}Co_{25}$ alloy is shown in Figure 6. At this composition, there is a Bader charge transfer of 0.40 e$^-$ from Co to Pd to fulfil the 4*d* states of Pd. In this way, the main electronic structure of the majority spin is fully filled and the Fermi level (E_F) falls in a valley of states in the electronic structure of the minority spin, located in front of a localized 3*d* peaks of Co. This combined effect leads to a reduction of the density of states at E_F in comparison with pure *fcc* Pd.

The DOS value at E_F of several Pd-Co compositions as calculated with and without spin polarization are shown in Figure 7. For low Co content, the values without spin polarization (NP) are higher than pure Pd and do not satisfy the Stoner criterion. This might explain why the system is more stable with ferromagnetic ordering. Therefore, the density of states at E_F decreases with Co content because of the spin

polarization (SP). Full details of the DOS of all investigated compositions and the SQS mixing energy are given in SI.
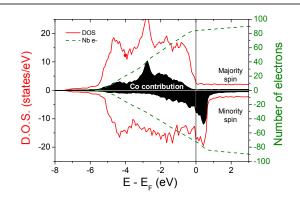

Figure 6. Total density of states (left hand side scale, red) and number of electrons (right hand side scale, green) of the *fcc* $Pd_{75}Co_{25}$ of 16-atom SQS-cell in the two directions of spin. The Co contribution in the DOS is represented by the black shaded region.
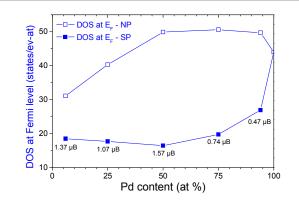

Figure 7. Density of states at E_F with (full symbols) and without (empty symbols) spin polarization, NP and SP respectively for the *fcc* phase Pd-Co treated by 16-atom SQS-cell. The magnetic moment by Co atom is indicated below SP points.

Discussions

It is important to compare these experimental findings to earlier results obtained on similar bulk Pd-Co compositions. The plateau pressures of hydride formation for bulk Pd-Co alloys are higher than that of pure Pd (decrease of the -ΔH_{abs}). Moreover, these plateaus are sloppy and the slope increases with Co content.[2] The slope and consequently the hysteresis between absorption and desorption plateau pressures are reduced by annealing and preparation of more homogenous alloys as well as by extensive cycling of bulk alloys.[3,4] However, the effects of the nature and concentration of solute atoms in Pd on the sloping plateau are not straightforward.

In the case of hydride forming $Pd_{90}Co_{10}$ nanoalloys (composites prepared at 500 and 600 °C), the plateaus start around 5 kPa and due to the sloping shape both samples are not fully hydrogenated 0.1 MPa. This indicates an increase of the equilibrium pressure in nanoalloys as compared to pure Pd

(plateau pressure around 2 kPa at 20 °C), in agreement with bulk Pd-Co substitutional alloys.

The sloping of plateau in the PCI curve is a typical feature of nanosized/nanoconfined Pd: the plateau becomes steeper with decreasing the particle size.[19,17,15] Several explanations have been suggested for Pd nanoparticles: broad size distribution of nanoparticles *via* size-related changes in surface tension, interface stress due to stabilizers/scaffolds or structural heterogeneities of the particles. The origin of the sloping plateau for Pd-Co nanoalloys is even more difficult to assess since both nanosizing/nanoconfinement and alloying effects are involved. Nevertheless, as a consequence of steep plateaus, both $Pd_{90}Co_{10}$ nanoalloys with average particle sizes of 6.4 and 23 nm are not fully transformed into the hydride phase at 0.1 MPa. Higher pressure is needed for full hydrogenation of these nanoparticles, as confirmed by two different experimental techniques. The PCI curves suggest also that the slope is size-dependent: the smaller the nanoparticles size, the steeper the plateau.

Based on *in situ* XRD analyses of $Pd_{90}Co_{10}$ nanoalloys with particle sizes of 6.4 and 23 nm, 34% and 5% of α phase are still present at 0.1 MPa, respectively. From the PCI curves, the capacities at 0.1 MPa are around 0.26 and 0.46 H/M for these two nanoalloys. Thus, it is possible to estimate the capacities of both $Pd_{90}Co_{10}$ nanoalloys at full hydrogenation (the nanoalloy is fully transformed into the hydride phase). The calculated values are 0.39 and 0.48 H/M for the $Pd_{90}Co_{10}$ nanoalloys with average particles size 6.4 and 23 nm, respectively. This result suggests that the hydrogen capacities of the hydride forming $Pd_{90}Co_{10}$ nanoalloys are size-dependent: the smaller the nanoparticle size, the lower the storage capacity (lower hydrogen solubility in the hydride phase), in agreement with pure Pd nanoparticles.[15,17,19,27]

As concerns the $Pd_{90}Co_{10}$ nanoalloy prepared at 300 °C (average size 2.4 nm), the formation of the hydride phase could not be confirmed either by PCI or *in situ* XRD measurements. Therefore, we hypothesis that this $Pd_{90}Co_{10}$ nanoalloy forms a solid solution with hydrogen at 20 °C. From the PCI curves of $Pd_{90}Co_{10}$ series, the hydrogen solubility in the α phase is a size-dependent parameter: the smaller the nanoalloys size, the higher the hydrogen solubility in the α phase. This trend is characteristic for nanosized Pd particles.[17,19]

In the same way, the $Pd_{75}Co_{25}$ nanoalloy series that forms solid solutions up to 0.1 MPa, show higher hydrogen solubilities with decreasing the particle dimensions: 0.33, 0.08 and 0.05 H/M for 12.5, 5.3 and 2.1 nm average particles sizes, respectively. Although, this increase in capacity with decreasing the particle size might also be due to nanoparticle surface effects: hydrogen adsorption on developed surfaces of small particles and/or cooperative phenomena between particles and carbon porous host might occur at room temperature.

In the case of Pd particles, nanosizing/nanoconfinement effects are obvious for sizes below 10 nm.[15] Similar effect is likely to occur in the present Pd-Co nanoalloys. Therefore, it is reasonable to compare the hydrogen storage capacity of Pd-Co

nanoalloys larger than 10 nm to bulk counterparts. Our results showed that Co substitution in Pd drastically decreases the hydrogen sorption capacity from 0.67, 0.48 to 0.05 H/M from pure Pd, $Pd_{90}Co_{10}$ (23 nm) to $Pd_{75}Co_{25}$ (12.5 nm).

The DFT calculations have been done on bulk *fcc* phase, neglecting nanoscale effects. However, they describe a general electronic behavior of Pd-Co alloys that might explain the composition-dependence of hydrogen sorption properties. The evolution of the DOS at E_F in *fcc* phase Pd-Co (Figure 7) is dissimilar to the simple approach of rigid band model. This model explained rather satisfactory the E_F shift in the non-magnetic Pd-*TM* systems (*TM* = Rh, Ag, Ir, Cu) and the formation of unoccupied states that is favorable to hydrogen uptake.[7,34] Within this simple model, an increase of the electronic unoccupied states with Co content is expected (since the number of valence electrons of Co is lower than Pd). However, the contribution of magnetism leads to a change of the spin population by an increase of the ferromagnetic states with Co content (see magnetic moment calculated at 0 K in Figure 7). This leads to the formation of a new localized peak after E_F in the minority spin population, which can be hardly filled with electrons from dissolved hydrogen atoms (Figure 6). This result confirms the observed experimental drastic reduction of the hydrogen absorption capacity in Pd-Co nanoalloys with Co content.

Conclusions

Well dispersed Pd-Co nanoalloys embedded into mesoporous carbon hosts have been prepared by direct and indirect synthetic methods. Two different series with Pd-rich compositions have been studied: $Pd_{90}Co_{10}$ and $Pd_{75}Co_{25}$. The average nanoparticle size can be tuned by both the temperature of the thermal treatment during synthesis and the chemical composition of alloy: the higher treatment temperature and richer Pd composition, the larger nanoparticle size. As a consequence, the combined effect of alloying and nanosizing/nanoconfinement on the hydrogen sorption properties of Pd-Co nanoparticles can be assessed.

From PCI curves and *in situ* XRD measurements at room temperature, a clear size-dependence of hydrogen sorption properties was evidenced. Among all composites, only $Pd_{90}Co_{10}$ nanoparticles with average particle sizes of 23 and 6.4 nm absorb hydrogen forming a hydride phase. All other nanoalloys show only the formation of solid solutions with hydrogen. The equilibrium pressure of hydride forming $Pd_{90}Co_{10}$ nanoalloys is higher, as compared to pure Pd and the slope of plateau is steeper with decreasing the nanoparticle size. Moreover, the hydrogen capacities of both hydride forming $Pd_{90}Co_{10}$ nanoalloys are size-dependent: the smaller nanoparticle size, the lower storage capacity. All nanoalloys forming solid solutions up to 0.1 MPa, show higher hydrogen solubility in the α phase with decreasing the particle dimensions.

Our results confirmed that Co substitution in Pd nanoalloys drastically decreases the hydrogen sorption capacity, as also demonstrated by SQS+DFT calculations.

These results are definitely important for the design of innovative nanomaterials for hydrogen storage as well as for heterogeneous catalysis, since Pd-based supported nanoparticles are widely used in the latter research field for chemical reactions involving hydrogen.[35]

Acknowledgements

References

1 Lewis F. A, *Platin. Met. Rev.*, 1982, **26**, 121–128.

2 R. Feenstra, D. Degroot, R. Griessen, J. Burger and A. Menovski, *J. -Common Met.*, 1987, **130**, 375–386.

3 T. B. Flanagan, D. Wang and H. Noh, *J. Alloys Compd.*, 1997, **253**, 216–220.

4 D. Wang, K. Y. Lee, S. Luo and T. B. Flanagan, *J. Alloys Compd.*, 1997, **252**, 209–218.

5 D. F. Teter and D. J. Thoma, *Metall. Mater. Trans. B-Process Metall. Mater. Process. Sci.*, 2000, **31**, 667–673.

6 S. Akamaru, T. Matsumoto, M. Hara, K. Nishimura, N. Nunomura and M. Matsuyama, *J. Alloys Compd.*, 2013, **580**, S102–S104.

7 S. Akamaru, M. Hara and M. Matsuyama, *J. Alloys Compd.*, 2014, **614**, 238–243.

8 M. Hara, H. Fujinami, S. Akamaru, N. Nunomura, K. Watanabe, K. Nishimura and M. Matsuyama, *J. Alloys Compd.*, 2013, **580**, S202 – S206.

9 P. E. de Jongh and P. Adelhelm, *Chemsuschem*, 2010, **3**, 1332–1348.

10 A. Pundt, M. Suleiman, C. Bahtz, M. T. Reetz, R. Kirchheim and N. M. Jisrawi, *Mater. Sci. Eng. B-Solid State Mater. Adv. Technol.*, 2004, **108**, 19–23.

11 C. Zlotea, F. Cuevas, V. Paul-Boncour, E. Leroy, P. Dibandjo, R. Gadiou, C. Vix-Guterl and M. Latroche, *J. Am. Chem. Soc.*, 2010, **132**, 7720–7729.

12 C. Zlotea, R. Campesi, F. Cuevas, E. Leroy, P. Dibandjo, C. Volkringer, T. Loiseau, G. Féréy and M. Latroche, *J. Am. Chem. Soc.*, 2010, **132**, 2991–2997.

13 W. Zhao, V. Fierro, C. Zlotea, M. T. Izquierdo, C. Chevalier-Cesar, M. Latroche and A. Celzard, *Int. J. Hydrog. Energy*, 2012, **37**, 5072–5080.

14 P. Dibandjo, C. Zlotea, R. Gadiou, C. M. Ghimbeu, F. Cuevas, M. Latroche, E. Leroy and C. Vix-Guterl, *Int. J. Hydrog. Energy*, 2013, **38**, 952–965.

15 C. Zlotea and M. Latroche, *Colloids Surf. Physicochem. Eng. Asp.*, 2013, **439**, 117–130.

16 P. E. de Jongh, M. Allendorf, J. J. Vajo and C. Zlotea, *Mrs Bull.*, 2013, **38**, 488–494.

17 M. Yamauchi, R. Ikeda, H. Kitagawa and M. Takata, *J. Phys. Chem. C*, 2008, **112**, 3294–3299.

18 S. Bastide, C. Zlotea, M. Laurent, M. Latroche and C. Cachet-Vivier, *J. Electroanal. Chem.*, 2013, **706**, 33–39.

19 A. Pundt and R. Kirchheim, *Annu. Rev. Mater. Res.*, 2006, **36**, 555–608.

20 R. Campesi, F. Cuevas, E. Leroy, M. Hirscher, R. Gadiou, C. Vix-Guterl and M. Latroche, *Microporous Mesoporous Mater.*, 2009, **117**, 511–514.

21 B. Mierzwa, Z. Kaszkur, B. Moraweck and J. Pielaszek, *J. Alloys Compd.*, 1999, **286**, 93–97.

22 K. Oishi and O. Savadogo, *Electrochimica Acta*, 2013, **98**, 225–238.

23 M. A. Matin, J.-H. Jang and Y.-U. Kwon, *J. Power Sources*, 2014, **262**, 356–363.

24 C. M. Ghimbeu, J.-M. L. Meins, C. Zlotea, L. Vidal, G. Schrodj, M. Latroche and C. Vix-Guterl, *Carbon*, 2014, **67**, 260 – 272.

25 A. Jahel, C. M. Ghimbeu, L. Monconduit and C. Vix-Guterl, *Adv. Energy Mater.*, 2014, **4**, 1400025.

26 C. M. Ghimbeu, M. Soprony, F. Sima, C. Vaulot, L. Vidal, J.-M. Le Meins and L. Delmotte, *Rsc Adv.*, 2015, **5**, 2861–2868.

27 C. M. Ghimbeu, C. Zlotea, R. Gadiou, F. Cuevas, E. Leroy, M. Latroche and C. Vix-Guterl, *J. Mater. Chem.*, 2011, **21**, 17765–17775.

28 A. Zunger, S. H. Wei, L. G. Ferreira and J. E. Bernard, *Phys Rev Lett*, 1990, **65**, 353.

29 C. Wolverton, *Acta Mater*, 2001, **49**, 3129–3142.

30 G. Kresse and J. Hafner, *Phys Rev B*, 1993, **47**, 558–561.

31 G. Kresse and D. Joubert, *Phys Rev B*, 1999, **59**, 1758.

32 J. P. Perdew, K. Burke and M. Ernzerhof, *Phys Rev Lett*, 1997, **78**, 1396.

33 Y. Oumellal, C. Zlotea, S. Bastide, C. Cachet-Vivier, E. Leonel, S. Sengmany, E. Leroy, L. Aymard, J.-P. Bonnet and M. Latroche, *Nanoscale*, 2014, **6**, 14459–14466.

34 S. Akamaru, M. Hara, N. Nunomura and M. Matsuyama, *Int. J. Hydrog. Energy*, 2013, **38**, 7569–7575.

35 C. Zlotea, F. Morfin, T. S. Nguyen, N. T. Nguyen, J. Nelayah, C. Ricolleau, M. Latroche and L. Piccolo, *Nanoscale*, 2014, **6**, 9955–9959.